


Article

Environmental Applications of Zeolites: Hydrophobic Sn-BEA as a Selective Gas Sensor for Exhaust Fumes

Martin Jendrlin ^{1,*} , Julien Grand ², Louwanda Lakiss ², Florent Dubray ², Philippe Bazin ², Jaafar El Fallah ², Svetlana Mintova ² and Vladimir Zholobenko ¹

¹ School of Chemical and Physical Sciences, Keele University, Keele ST5 5BG, UK

² Laboratoire Catalyse et Spectrochimie, ENSICAEN, CNRS, Normandie Université, 6 Bd Maréchal Juin, 14000 Caen, France

* Correspondence: m.jendrlin@keele.ac.uk

Abstract: Environmental monitoring of pollutants, such as NO_x and CO_x, which can be facilitated by a range of gas sensors, is of considerable fundamental and practical importance. This work has been focused on the synthesis and evaluation of zeolite β with tin (Sn-BEA) and dealuminated β (DeAl-BEA) zeolites. The zeolite samples have been extensively investigated by IR, UV-VIS and NMR spectroscopy, XRD, TGA, and N₂ adsorption-desorption. The prepared Sn-BEA sample is characterised by the submicron particle size, an almost defect-free structure, and high hydrophobicity. Sensors containing selective microporous layers based on Sn-BEA and DeAl-BEA zeolites have been prepared and extensively tested. Both the Sn-BEA and DeAl-BEA zeolites have been deposited in thin films and evaluated as gas sensors for CO, CO₂, NO, and NO₂ in the presence of water vapour at room temperature. The Sn-BEA zeolite-based sensor showed high selectivity towards NO₂, while the DeAl-BEA is selective towards CO₂ and NO₂.

Keywords: zeolites; BEA; layers; FTIR; gas sensors



Citation: Jendrlin, M.; Grand, J.; Lakiss, L.; Dubray, F.; Bazin, P.; El Fallah, J.; Mintova, S.; Zholobenko, V. Environmental Applications of Zeolites: Hydrophobic Sn-BEA as a Selective Gas Sensor for Exhaust Fumes. *Chemistry* **2023**, *5*, 334–347. <https://doi.org/10.3390/chemistry5010025>

Academic Editors: José Antonio Odriozola and Hermenegildo García

Received: 18 January 2023

Revised: 15 February 2023

Accepted: 16 February 2023

Published: 21 February 2023



Copyright: © 2023 by the authors. Licensee MDPI, Basel, Switzerland. This article is an open access article distributed under the terms and conditions of the Creative Commons Attribution (CC BY) license (<https://creativecommons.org/licenses/by/4.0/>).

1. Introduction

In the contemporary world, air pollution is a growing problem that presents a significant threat to human health. Combustion engines and gas exhaust fumes are key sources of pollutants [1,2]. Exhaust fumes consist mostly of harmless O₂, N₂, and water vapour (up to 80%), but CO₂, CO, NO_x, and SO_x are produced in quantities sufficient to cause negative environmental and health effects [3]. Reports from major environmental governing bodies mainly focus on the control of NO_x, SO_x, O₃, and CO in addition to fine particulate matter [2,4]. Therefore, effective monitoring of these gases employing a range of gas sensors is required.

Gas sensors utilise a variety of physical and chemical phenomena to detect species of interest. Over 50% of the market share is represented by electrochemical, semiconductor, and infrared-based gas sensors [5]. Electrochemical sensors utilise solid electrolytes, such as yttria-stabilised zirconia, as the main active components in a galvanic cell [6,7]. The amperometric response of the cell is related to the concentration of the specified gas. This type of sensor has found the most important application as the oxygen sensor in gas exhaust systems. However, electrochemical sensors for most gas analyses lack long-term stability and selectivity if oxygen is present as the main interfering gas [6,7]. Semiconductor sensors utilise the conductometric response of a variety of metallic oxides (TiO₂, WO₃, ZrO₂, SnO₂) [8–10] with SnO₂ being most common as it is responsive towards CO, NO₂, and NH₃ [8–10]. However, these sensors require high operating temperatures (>150 °C), and in the presence of oxygen, they also often lack selectivity [8–10]. These characteristics could be optimised either by the incorporation of noble metals or by mixing several types of oxides; however, such modifications lead to a rise in manufacturing costs. Most of the widely available infrared sensors are based on non-dispersive infrared technology [11].

These sensors are characterised by low power consumption, but the poor detection limits and water interference present a major problem [11].

Zeolites are one type of material that could enhance the selectivity of gas sensors. Zeolites are highly-ordered crystalline microporous aluminosilicates. They are also widely used as molecular sieves and industrial catalysts, and also in water treatment [12]. The porosity and high adsorption capacity of zeolites make them viable materials for gas sensor applications [13–16]. Zeolites have been utilised both as active sensing components and as auxiliary phases (e.g., filter or sieving layer or an immobilisation template) [14,15]. As active sensing components, zeolites have been mostly used in gas sensors that are based on ion conductivity, potentiometry, and cataluminescence [14,15]. Sensing properties of zeolite may be dependent on the metal ions present in the zeolite pores. An alternative way of zeolite modification is by isomorphous substitution, that is incorporating other metals (Ti, Ga, Zr, Sn) [17–22] into the framework structure instead of aluminium. These metal-containing zeolites are extensively used in heterogeneous catalysis, including some of the commercially exploited framework types, such as BEA, MFI, CHA, and FAU [22–31]. For instance, Sn-containing BEA zeolites are highly selective catalysts in biomass conversion: enhanced activity and product selectivity were reported in Meerwin–Pondorf–Verlein reduction [20], Baeyer–Villiger oxidation [22], sugar isomerisation [23–28], and epimerisation [23,32]. Optimised synthetic procedures resulted in the preparation of highly crystalline, nearly defect-free Sn-BEA materials [22,33–35]. Their superior catalytic activity is attributed to Lewis acid sites associated with the Sn atoms incorporated in the zeolite framework. Unlike in SnO₂, where Sn is octahedrally coordinated, in zeolites, Sn is tetrahedrally coordinated [22,36–39]. The tetrahedrally coordinated Sn atoms are observed in two main forms that are referred to as open and closed sites. Closed sites correspond to Sn(OSi)₄ and open sites correspond to Sn(OSi)₃(OH) species [35,38]. In addition, a 3-dimensional network of channels with 12-membered ring apertures offers good accessibility to a variety of species.

Although Sn-BEA zeolites have been widely utilised in catalysis and pure SnO₂ in gas sensors, to the best of our knowledge, no application of Sn-BEA for gas sensors has been reported. In this work, we explore the potential of combining the sensing properties of Sn-based compounds with the zeolite pore confinement effects aiming to produce a new type of selective gas sensors. A hydrophobic Sn-BEA zeolite has been synthesised and characterised using a range of physicochemical techniques. A prototype Sn-BEA-based sensor has been prepared and tested under realistic operating conditions. Our research demonstrates the potential of this material as a NO₂-selective gas sensor for the analysis of exhaust gases in the presence of CO, CO₂, O₂, and H₂O.

2. Materials and Methods

Zeolite synthesis. Zeolite preparations followed the procedure from Ref [35]. In a typical experiment, 5 g of commercial BEA (Zeolyst, Conshohocken, PA, USA, Si/Al = 19.0) was dealuminated in 125 mL of concentrated nitric acid (HNO₃, 68%, Fisher Scientific, Loughborough, UK) for 16 h at 80 °C. Subsequently, the dealuminated BEA (deAl-BEA) sample was washed 6 times with 25 mL deionized water (Elga Purewater system, Cambridge, UK, <0.067 μS/cm) and dried overnight. The as-prepared deAl-BEA was used as a seed material in further steps. The synthesis gel was prepared by mixing 6.98 g of tetraethylorthosilicate (Si(OC₂H₅)₄, Sigma Aldrich, Gillingham, UK) and 7.67 g of tetraethylammonium hydroxide ((C₂H₅)₄N(OH), 40%, Sigma Aldrich, Gillingham, UK). Subsequently, 0.12 g of tin (IV) chloride pentahydrate (SnCl₄·5H₂O, Sigma Aldrich, Gillingham, UK) was dissolved in 0.6 mL water and added dropwise to the gel. The Si/Sn molar ratio in the gel was 100. The gel was stirred for 12 h in a closed container and then for 3 days in an open container. After allowing the excess water and ethanol to evaporate, 0.74 g of hydrofluoric acid (HF, 48%, Sigma Aldrich, Gillingham, UK) was added to the gel. The gel was homogenised and 0.085 g of deAl-BEA seeds in 0.58 g of water was added and mixed thoroughly. The prepared gel was heated in an autoclave for 6 days at 140 °C. The products were then removed from the autoclave and washed 5 times with 25 mL of water, followed by washing 5 times using 25 mL acetone (VWR Chemicals, Lutterworth, UK). Samples were dried overnight and

a part of the sample was calcined in a muffle furnace for 1 h at 400 °C in a nitrogen flow, followed by calcination for 5 h at 550 °C in an oxygen flow (Figure S1).

Zeolite characterization. Zeolite samples were characterised by X-ray powder diffraction (Bruker D8 Advance diffractometer, Durham, UK, Cu K α at 40 kV and 40 mA, $2\theta = 5\text{--}60^\circ$), scanning electron microscopy (Hitachi TM 3000, London, UK, with Bruker EDX system at 500 \times magnification, 300 s EDX data collection time), N₂ adsorption-desorption (Micrometrics Model ASAP2020), solid-state MAS NMR (Bruker Avance III-HD 500, 11.7 T, operating at 99.3 MHz, using a zirconia rotor of 4 mm outer diameter spun at 12 kHz), thermogravimetric analysis (Rheometric Scientific STA, Epsom, UK, 1500, 20–800 °C, 10 °C/min, 40 mL/min N₂ flow), and FTIR (Thermo, Loughborough, UK, iS10 spectrometer with a custom-made cell, 6000–1000 cm⁻¹, 64 scans, 4 cm⁻¹ resolution, transmission mode).

Prior to FTIR characterisation, zeolite samples were pressed into self-supported pellets (13 mm diameter, 10–15 mg). Activation was carried out in a vacuum system at 450 °C (ramp rate 1 °C/min, <10⁻⁵ Torr), then the sample was cooled to ambient temperature under vacuum, and its IR spectrum was collected. Pyridine characterisation was conducted according to Ref [40,41]. Following the activation procedure, the sample was kept at 150 °C, and small portions of pyridine (C₅H₅N, Arcos Organics, Geel, Belgium, 99.5%, dried over 3A molecular sieve) were introduced into the cell until the saturation of the acid sites was achieved. Physisorbed pyridine was removed by evacuation at 150 °C. Omnic software (Thermo, Loughborough, UK) was used to analyse the obtained spectra. The molar absorption coefficients were $\epsilon(\text{Py-B}) = 1.26 \text{ cm}^2/\mu\text{mol}$ and $\epsilon(\text{Py-L}) = 1.79 \text{ cm}^2/\mu\text{mol}$, according to Ref. [41]

For ²⁹Si MAS NMR, a single pulse excitation (30° flip angle) was used with a recycle delay of 30 s. For ¹H/²⁹Si CP-MAS NMR, a contact time of 5 ms and a recycle delay of 2 s were used, respectively. Chemical shifts were referenced to tetramethylsilane (TMS). All MAS NMR spectra were recorded using a 4mm MAS probe-head at a spinning rate of 12 kHz. Adsorption of trimethylphosphine oxide (TMPO, (CH₃)₃PO, Aldrich, Gillingham, UK) as a probe-molecule was followed by ³¹P NMR under ¹H decoupling. Samples were dehydrated at 400 °C under vacuum ($\sim 4 \times 10^{-5}$ Torr) while a solution of TMPO in dichloromethane was prepared. TMPO solution was added to the dehydrated zeolite sample under an argon atmosphere in a glovebox, and the resulting suspension was treated in an ultrasonic bath for 15 min. The suspension was dried by evaporating the solvent under vacuum for 2 h. The TMPO-loaded zeolites were then packed in zirconium rotors for the NMR characterisation. ³¹P $\pi/2$ and π -pulses lengths were 7 and 14 μs , respectively, for all measurements.

Sensor preparation. Sensors were made according to the procedure described in Ref [42]. Silicon wafers were cut into 10 \times 10 mm squares and cleaned with ethanol (95%, VWR chemicals, Lutterworth, UK) and acetone. As-prepared zeolite samples were dispersed in acetone (4 wt%), mixed with 3-propylcellulose as a binder, and deposited on silicon wafers (10 \times 10 mm) by spin coating (Laurell spin coater, Horsham, PA, USA, model WS-400B-6NPP-LITE). Prepared films were then calcined for 30 min at 450 °C (ramp rate 5 °C/min).

Operando gas detection. Experiments testing the sensor performance were conducted using a custom-made IR operando cell in a flow system at 25 °C, with argon as a carrier gas containing 100 ppm of water (1 bar, 25 cm³/min). Prior to the controlled adsorption of individual gas mixtures (20 to 5000 ppm of CO, CO₂, NO, or NO₂ in Ar), the samples were activated in situ at 250 °C for 30 min (ramp rate 3 °C/min) and cooled down to the ambient temperature. The spectra were collected using a Thermo iS50 spectrometer, Loughborough, UK, equipped with an MCT detector, using 64 scans at 4 cm⁻¹ resolution in the 6000–1000 cm⁻¹ spectral range. All presented sensor performance data are the difference spectra obtained by subtraction of the zeolite spectrum prior to the gas adsorption experiment from the spectrum of a sample at a specific concentration of the target gas. Since some water vapour was inherently present in the argon flow, gas-phase water correction was applied.

3. Results and Discussion

3.1. Physicochemical Characterization of Zeolite Samples

A summary of the elemental analysis data and textural properties of the parent BEA, dealuminated BEA (DeAl-BEA), and Sn-BEA samples is presented in Table 1. The SEM micrographs are shown in Figures S2–S4. Particle aggregates are in the range of 0.5–2 μm , which is considerably smaller than those reported in the literature (5–20 μm) [20–27,32,35–37,43–48]. Particles in the submicron range are necessary for the preparation of viable films for gas sensors. The obtained values agree with those reported in the literature [35], e.g., the attained Si/Sn ratio of 64 corresponds to 1.3% (calculated as $\text{Si}/(\text{Si} + \text{Sn}) \times 100\%$), which is marginally higher than the values of 0.25–1% reported for similar procedures [20–27,32,35–37,43–48].

Table 1. Summary of BEA-19, DeAl-BEA, and Sn-BEA characterisation data.

	BEA	DeAl-BEA	Sn-BEA
Si/Al ratio	19.2	497	1541
Si/Sn ratio	-	-	64
w (H ₂ O) (%)	16	14	1
Particle size (μm)	0.5–2	0.5–2	0.5–2
N ₂ ads-des (m ² /g)	640	572	504
BAS ($\mu\text{mol/g}$)	395	16	3
LAS ($\mu\text{mol/g}$)	106	6	20

XRD patterns of the parent BEA, DeAl-BEA, and Sn-BEA are presented in Figure 1. The collected patterns correspond to those previously reported in the literature [22,34,35]. Both DeAl-BEA and Sn-BEA maintain all the peaks characteristic of the BEA framework, and no other zeolite phases have been detected [49]. Based on the peak intensities at 5–9, 13–15, and 17–19° 2 θ , the ratio polymorph A: polymorph B is 0.6: 0.4 [49]. The peaks in the Sn-BEA pattern are well-defined as compared with those for BEA and DeAl-BEA, indicating a larger size of the crystalline domains. They are also shifted to lower 2 θ values relative to the parent zeolites, reflecting an increase in the lattice parameters because of Sn insertion into the framework. Peaks corresponding to the bulk SnO₂ phase (26.5, 33.8, 37.6, and 51.5° 2 θ) have not been observed in the pattern of freshly prepared Sn-BEA. However, a low-intensity peak (26.5° 2 θ) has been detected nine months after the sample preparation (Figure S5), which is probably due to the partial degradation of the Sn-containing framework via hydrolysis of Si-O-Sn bonds and eventual formation of SnO₂ clusters and Si-OH groups [43].

The DRUV-VIS spectra of Sn-BEA and DeAl-BEA zeolites are shown in Figure S6. The difference spectrum shows a peak at 230 nm, which is characteristic of the tetrahedral Sn atoms in the zeolite framework interacting with water molecules. A low-intensity peak around 290 nm indicates a minor contribution of SnO₂ in the sample [35,48]. These data further support a high level of Sn atoms substitution in the BEA structure rather than the presence of a mixture of SnO₂ and a siliceous zeolite.

The results of the thermogravimetric analysis are presented in Figure S7. Calcined Sn-BEA shows a negligible water loss (1%) compared with parent BEA (16%) and DeAl-BEA (14%) upon heating to 200 °C. The water loss for both BEA and DeAl-BEA is similar because of the presence of bridging OH-groups and silanols, both of which increase the degree of hydrophilicity. Importantly, this characterisation technique indicated the high level of hydrophobicity of the Sn-BEA sample, which would be a beneficial feature for a sensor operating in humid environments.

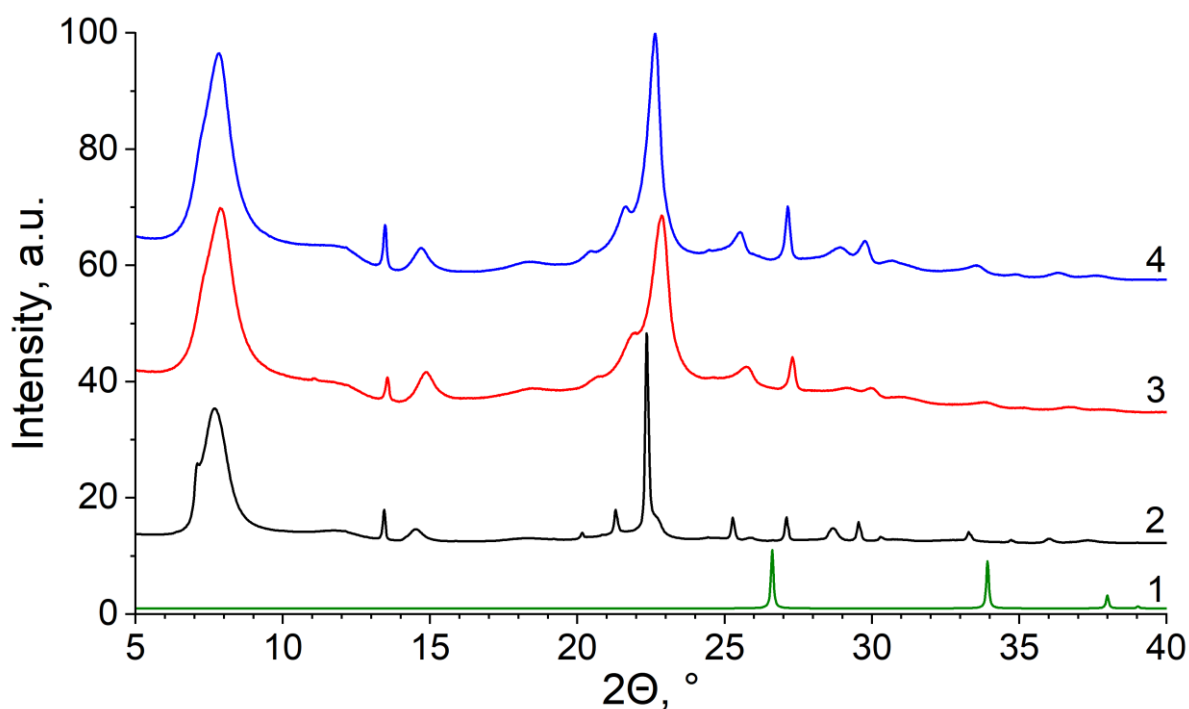


Figure 1. XRD patterns of SnO₂ (1), Sn-BEA (2), DeAl-BEA (3), and BEA (4); patterns are offset for clarity.

²⁹Si MAS NMR spectrum of Sn-BEA contains all peaks (−111.6, −112.2, −113.1, −115.7 ppm) in the Q⁴ region (Figure 2). The well-defined narrow peaks in this region are indicative of a highly siliceous zeolite with very few structural defects in the framework [50]. In contrast, the spectrum of parent BEA zeolite shows relatively broad overlapping peaks in the regions corresponding to Q³ and Q⁴ species, such as Si(OAl)_x(OSi)_{4−x} or Si(OH)_x(OSi)_{4−x}, where x is 0 or 1 [28,37]. These samples have been further characterised using ²⁹Si-¹H cross-polarization (Figure S8). In the ²⁹Si-¹H CP MAS NMR spectrum of Sn-BEA, three ill-defined peaks (−104, −114, and −118 ppm) have been detected. These peaks correspond to the Q³ and Q⁴ regions of the spectrum [51]. However, the signal intensity is very low, which further confirms that there are almost no silanol groups present in the Sn-BEA sample.

In the ³¹P NMR spectrum of sample DeAl-BEA, only one low-intensity peak around 50 ppm is observed (Figure S9), which can be assigned to TMPO interacting with weak BAS, i.e., silanol groups [38,52,53]. No peak at this position is found for the Sn-BEA sample, further indicating that there are very few defects in the structure. The spectrum of TMPO adsorbed on Sn-BEA contains two distinct peaks, a low-intensity sharp peak at 43.2 ppm (associated with the physisorbed TMPO) and an intense asymmetric peak at 35.9 ppm (fwhm > 9 ppm), which results from an overlap of two peaks at 35.9 ppm and 40.8 ppm with an intensity ratio of approximately 3:1, as shown by the spectral deconvolution presented in Figure S10. The peaks at 35.9 ppm and 40.8 ppm could be assigned to TMPO interacting with weak LAS associated with Sn atoms in the zeolite framework. Their upfield shift could be also explained by the presence of residual F[−] ions in the BEA structure [23,38].

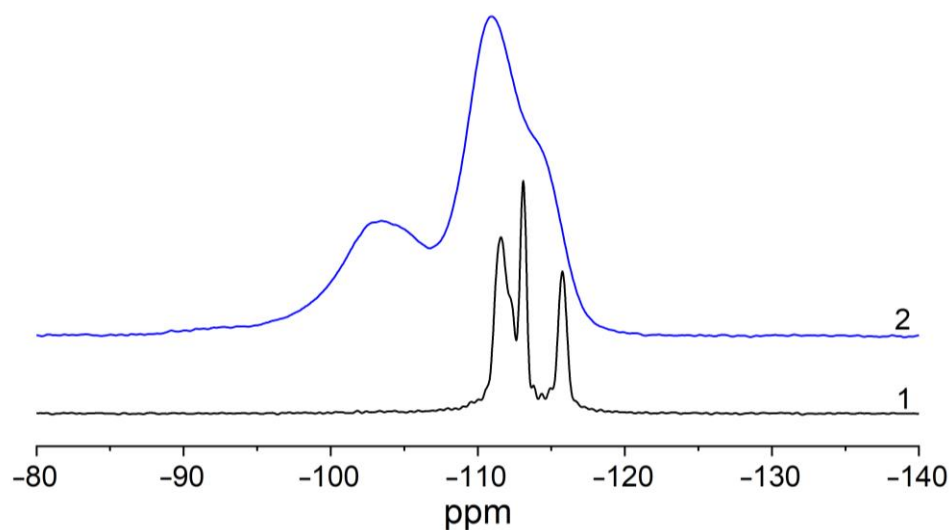


Figure 2. ^{29}Si MAS NMR spectra of Sn-BEA (1) and BEA (2) zeolite samples.

FTIR spectra of the zeolites before and after adsorption of Py are presented in Figures 3 and 4, and the number of BAS and LAS is summarised in Table 1. Most of the aluminium from the initial BEA sample was removed during the dealumination process, which has been confirmed by the elemental analysis (Table 1). Following this procedure, “silanol nests” are generated in the parts of the structure where aluminium is removed, which can be observed in the $3800\text{--}3500\text{ cm}^{-1}$ region, as the peak corresponding to Si-OH groups ($\sim 3740\text{ cm}^{-1}$ for BEA and $\sim 3727\text{ cm}^{-1}$ for DeAl-BEA) broadens and increases in intensity as compared with the parent sample due to hydrogen bonding within the newly formed silanol nests (Figure 3). The number of B-Py ($\sim 1545\text{ cm}^{-1}$) and L-Py ($\sim 1455\text{ cm}^{-1}$) complexes detected via Py adsorption on the parent BEA-19 is 395 and 106 $\mu\text{mol/g}$, but only 16 and 6 $\mu\text{mol/g}$ on the DeAl-BEA, confirming successful dealumination of the original zeolite. For Sn-BEA, the number of detected BAS is less than 3 $\mu\text{mol/g}$, indicating almost a complete loss of OH-groups in the structure during the fluoride-mediated synthesis, whereas the number of LAS has increased to 20 $\mu\text{mol/g}$ in comparison with the DeAl-BEA sample. Note that the number of Sn atoms introduced into Sn-BEA is 1.5% of T atoms. Importantly, the peak position of the Py-L complexes has shifted from 1455 cm^{-1} for BEA to 1450 cm^{-1} for Sn-BEA (Figure 4), which corresponds to Py interacting with weak LAS [41]. All these data are indicative of tin incorporation into the BEA framework [37]. The difference FTIR spectra (Figures S11 and S12) show negative peaks in the $3600\text{--}3800\text{ cm}^{-1}$ region. The negative peak of low intensity at $\sim 3741\text{ cm}^{-1}$ for Sn-BEA results from Py interaction with a small number of external silanols. For DeAl-BEA, the negative peak at 3728 cm^{-1} (with a shoulder at $\sim 3741\text{ cm}^{-1}$) is due to Py interacting mostly with internal and some external silanol groups. This could be explained by inserting Sn atoms in the “silanol nests” in the framework of DeAl-BEA, used as the seed material, which is in accordance with the TG and NMR data, hence confirming that the Sn-BEA sample is largely silanol-free and, thus, hydrophobic.

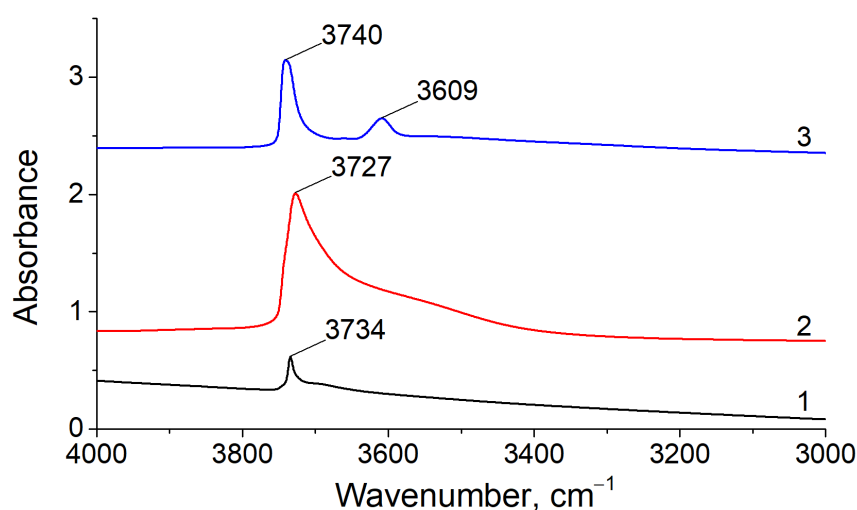


Figure 3. FTIR spectra of Sn-BEA (1), DeAl-BEA (2), and BEA (3) before Py adsorption; spectra are offset for clarity.

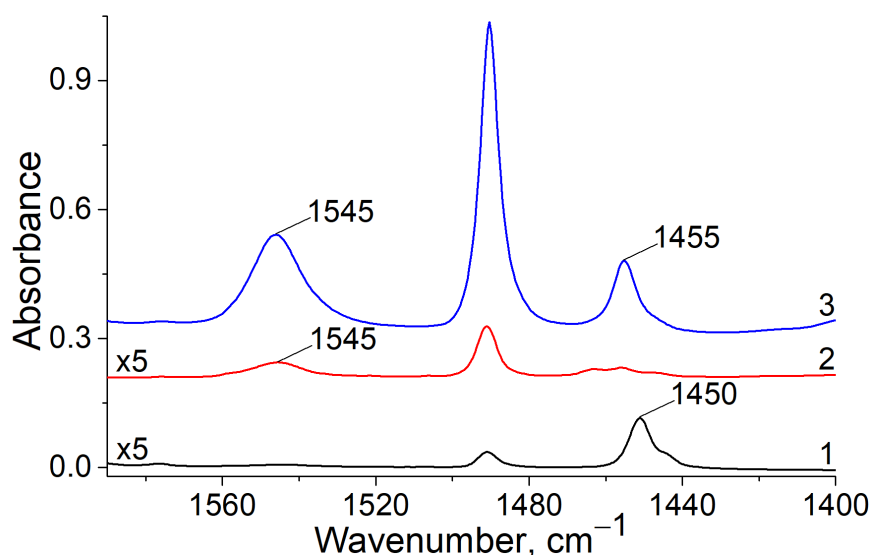


Figure 4. FTIR spectra of Sn-BEA (1), DeAl-BEA (2), and BEA (3) following the Py adsorption; spectra are offset for clarity.

3.2. Detection of CO, CO₂, NO, NO₂ by Sn-BEA and DeAl-BEA Zeolite-Based Sensors

The response of the prototype sensors based on Sn-BEA and the parent DeAl-BEA zeolites towards adsorption of specific gases and water vapour has been monitored by operando FTIR and the data are presented in Figures 5, 6 and S14–S25. Samples were tested in argon stream, as a model system for real-life conditions. Similar approaches have been reported previously [13,54,55]. Additionally, the XRD patterns in Figure S5 confirm that the sample exposed to ambient conditions (H₂O, O₂) for nine months had only a minor deterioration. The water quantity present in the carrier gas should not affect the adsorption properties of the target gases because of the hydrophobic nature of the studied material [55].

Both Sn-BEA and DeAl-BEA have shown selective response towards NO₂, (Figures 5, 6, S17 and S22), while the DeAl-BEA has also been responsive to CO₂ (Figures S19 and S20). When no significant gas adsorption is observed, e.g., for CO and NO, mostly the peaks corresponding to the gas phase of the used target gas and water vapour have been observed, along with the peaks in the 1620–1640 cm⁻¹ region assigned to the bending vibration mode of water adsorbed on the zeolite surface [56]. As mentioned previously, the adsorbed water stems from the water vapour introduced into the carrier gas to provide a more realistic model of the tested gas flows. For the adsorption

of CO₂ on DeAl-BEA (Figures S19 and S20), the peak observed at 2344 cm⁻¹ is ascribed to physisorbed CO₂, probably on the surface OH-groups [56]. Since this peak is overlaying with the gas phase peaks of CO₂, the gas phase correction was applied to quantify the data (Figure S20).

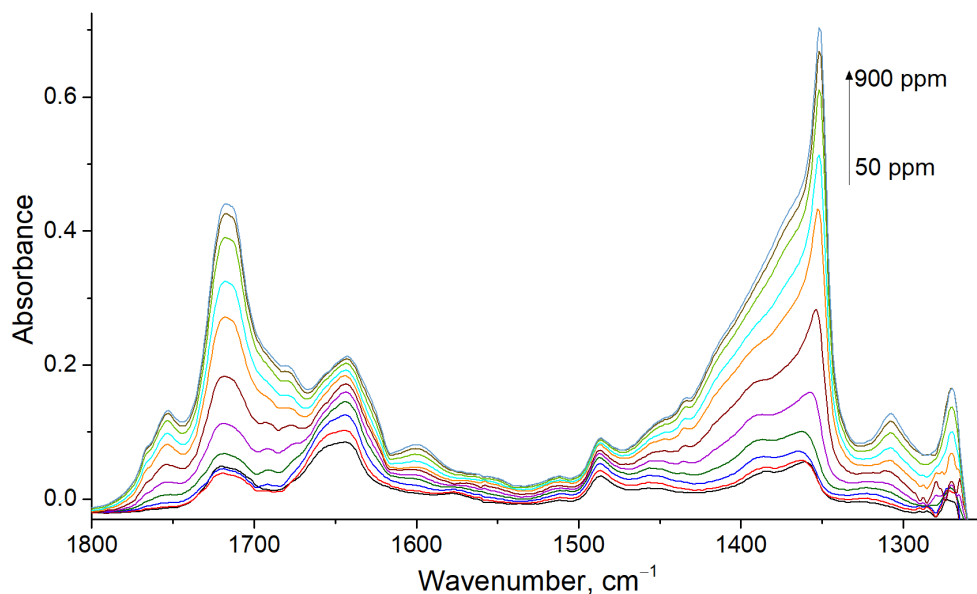


Figure 5. FTIR spectra of NO₂ detected by Sn-BEA: 50 ppm (black), 75 ppm (red), 100 ppm (blue), 200 ppm (green), 300 ppm (purple), 400 ppm (dark red), 500 ppm (orange), 600 ppm (light blue), 700 ppm (light green), 800 ppm (brown), 900 ppm (silver).

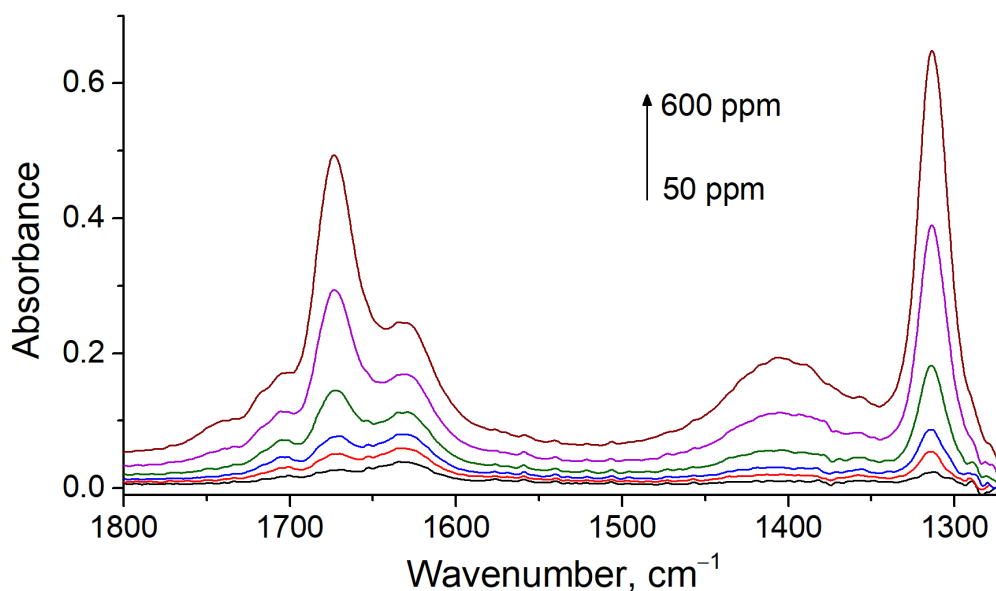


Figure 6. FTIR spectra of NO₂ detected by DeAl-BEA: 50 ppm (black), 75 ppm (red), 100 ppm (blue), 200 ppm (green), 400 ppm (purple), 600 ppm (dark red).

The most interesting result of these tests is the observed selective response of both Sn-BEA and DeAl-BEA towards NO₂. Two main regions of the spectrum containing distinctive peaks indicative of the interaction of the sensors with NO₂ are 1800–1600 cm⁻¹ (region A) and 1500–1300 cm⁻¹ (region B). In region A for Sn-BEA, only two peaks at 1645 and 1720 cm⁻¹ can be detected at lower concentrations (50–400 ppm). At 50 ppm of NO₂ the peak ratio is approximately 2:1, with the ratio decreasing as the concentration increases

to 400 ppm (Figure 5). At higher concentrations (>500 ppm), the peak at 1720 cm^{-1} becomes the most intense. Further peaks appear at 1600 and 1755 cm^{-1} , and a shoulder at 1685 cm^{-1} . For DeAl-BEA, only a band at 1630 cm^{-1} is found initially. As more NO_2 is introduced, additional peaks develop at 1670 and 1700 cm^{-1} (Figure 6). The peak at $\sim 1670\text{ cm}^{-1}$ is increasing in intensity with a peak at 1700 cm^{-1} merging as a shoulder to the central peak as the concentration of NO_2 increases. In region B for Sn-BEA, the main peaks are observed at ~ 1310 , 1360 (most intense with a broad shoulder) and 1485 cm^{-1} (Figure 5). For the DeAl-BEA sample, the major peaks are found at 1315 and 1405 cm^{-1} (Figure 6).

In agreement with the literature, the peaks appearing upon NO_2 adsorption can be attributed to the disproportionation of NO_2 in contact with solid catalysts, resulting in the formation of a range of monodentate, bidentate or bridging NO^+ , NO_2^- , and NO_3^- species as well as more complex structures resulting from their transformations [57–59]. Since the Sn-loading of Sn-BEA is relatively low, the formation of bridging species could be excluded. Furthermore, as no peaks have been detected in the $2200\text{--}2000\text{ cm}^{-1}$ region of the spectrum, the presence of $-\text{NO}^+$ and $-\text{NO}^+(\text{NO}_2)$ species on the samples prepared in this study should probably be ruled out [57,58]. Based on the NO_2 adsorption data for Sn-MFI and Fe-exchanged MFI and BEA zeolites, peaks in the $1800\text{--}1600\text{ cm}^{-1}$ region can be assigned to nitro-species bound to either Al or Sn. The peaks at $\sim 1760\text{--}1710\text{ cm}^{-1}$ are commonly attributed to N_2O_4 dimers [13,57–62]. This is in accord with their occurrence at higher concentrations of NO_2 . The peaks at $\sim 1645\text{ cm}^{-1}$ for Sn-BEA and 1630 cm^{-1} for DeAl-BEA could be interpreted as coordinated nitro-species; however, they can also originate from potentially overlapping peaks of adsorbed water, found in experiments with all the gases containing 100 ppm of water in the Ar flow (see Figures S23 and S24). The peak positions in region A for Sn-BEA are blue-shifted as compared with those for DeAl-BEA, Si-, and Sn-MFI. The peaks in region B can be attributed to nitrate or nitrite species [57–62]. Our interpretation is further confirmed by the room-temperature desorption experiments (Figures 7C and S25). Most peaks in region A are partially removed, which is characteristic of relatively weakly bound species, such as NO_2 or N_2O_4 . Indeed, the 1601 cm^{-1} peak disappeared instantly after stopping the NO_2 flow, while the intensity of other peaks, e.g., at 1645 cm^{-1} , decreases gradually. This could indicate that the latter peak results from a superposition of nitro-species and adsorbed water. The IR peaks in region B demonstrate only very minor changes throughout the desorption period, which can be attributed to subtle transformations of NO_3^- and NO_2^- , while the total peak area in the B region is virtually unchanged (Figure 7C), as would be expected for the nitrate and nitrite species [59]. The room-temperature stability of the peaks in the region B could suggest that the observed signal is due to NO_2 interacting with Lewis acid sites.

For the actual sensor performance, the areas of all peaks in a specific part of the spectrum, e.g., regions A and B, are more important since the portable IR sensors do not possess spectral resolution comparable to research-grade laboratory instruments [11]. Therefore, for the performance of a sensor, it is more useful to quantify the peak area of the “target” regions that corresponds to a specific concentration value. For Sn-BEA and DeAl-BEA, the absorption peaks of various N_xO_y species in both regions ($1800\text{--}1600$ and $1500\text{--}1300\text{ cm}^{-1}$) are evolving in a similar fashion (Figure 7A,B). The growth is not quite linear, and it is comparable to the Sn-MFI system [13]. As mentioned above, the peaks in the $1800\text{--}1600\text{ cm}^{-1}$ region can be partially removed upon desorption of NO_2 from the Sn-BEA at room temperature, while the peaks in the region 1500 to 1300 cm^{-1} cannot. Therefore, in the $1800\text{--}1600\text{ cm}^{-1}$ region, the sensor could be used to determine dynamic changes in the current concentration, while the $1500\text{--}1300\text{ cm}^{-1}$ region would allow to detect the maximum concentration of NO_2 in the monitored system during a certain period.

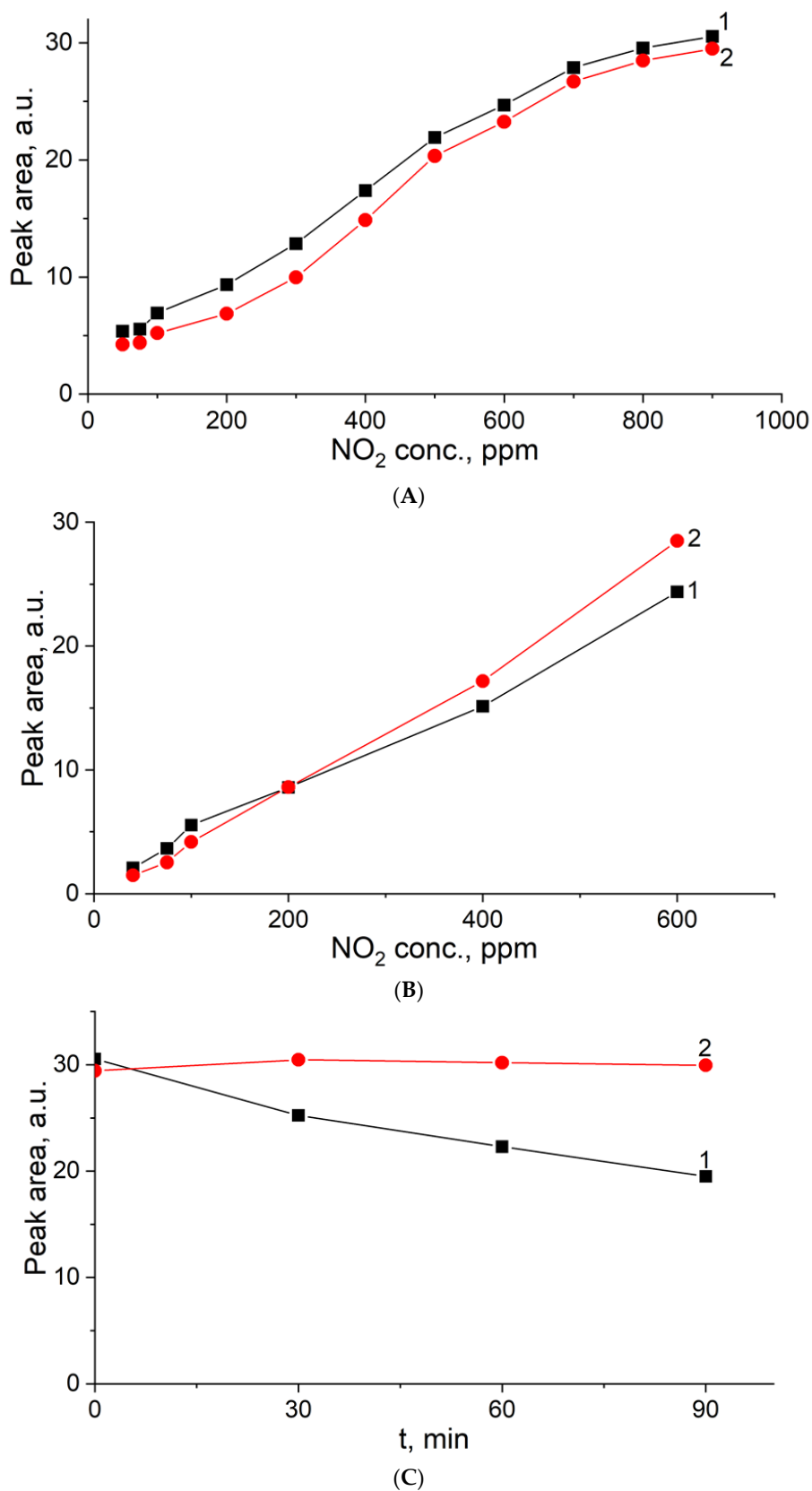


Figure 7. (A) Evolution of the IR peak areas following NO₂ detection by Sn-BEA zeolite: 1800–1600 cm⁻¹ (1), 1500–1300 cm⁻¹ (2). (B) Evolution of the IR peak areas following NO₂ detection by DeAl-BEA zeolite: 1800–1600 cm⁻¹ (1), 1500–1300 cm⁻¹ (2). (C) Evolution of the IR peak areas of NO₂ detection by Sn-BEA zeolite upon desorption in Ar flow at room temperature: 1800–1600 cm⁻¹ (1) and 1500–1300 cm⁻¹ (2).

4. Conclusions

In this study, sensors containing Sn-BEA and dealuminated BEA zeolites have been prepared. The zeolite samples have been extensively characterised by IR, UV-VIS and NMR spectroscopy, XRD, TGA, and N₂ adsorption-desorption. The prepared Sn-BEA sample revealed a nearly defect-free structure and high hydrophobicity alongside the submicron particle size. Sn-BEA has been utilised as an IR-based gas sensor at room temperature, and its performance has been compared with that of DeAl-BEA. Both sensors have been evaluated for their response to CO, CO₂, NO, and NO₂ in the presence of water vapours. Sn-BEA displays a selective response to NO₂, while DeAl-BEA responds to CO₂ and NO₂. Our data demonstrate the potential of zeolite BEA-based sensors to determine both the dynamic changes in current concentration of the analyte gas and the maximum concentration during a certain period. The future research should focus on the sensor performance studies under realistic conditions, including elevated temperatures and lower concentrations of the target gases.

Supplementary Materials: The following supporting information can be downloaded at: <https://www.mdpi.com/article/10.3390/chemistry5010025/s1>, Figure S1. Sn-BEA calcination scheme. Figure S2. SEM micrographs of BEA (left) and DeAl-BEA (right) zeolites. Figure S3. SEM micrographs of Sn-BEA zeolite. Figure S4. SEM micrographs of Sn-BEA powder (left) and Sn-BEA deposited on a silicon wafer (right). Figure S5. XRD patterns of Sn-BEA freshly prepared (1), Sn-BEA zeolites after 9 months (2). Figure S6. DRUV-VIS spectra of Sn-BEA (1) and DeAl-BEA (2) zeolites, (1)-(2) difference spectrum (3). Figure S7. TG curves of Sn-BEA (1), DeAl-BEA (2) and BEA (3) zeolites. Figure S8. ²⁹Si-1H CP MAS NMR spectra of Sn-BEA (1), and BEA (2) zeolites. Figure S9. ³¹P MAS NMR spectra of TMPO adsorbed on Sn-BEA (1) and DeAl-BEA (2, intensity is multiplied by a factor of 50) zeolites. Figure S10. Deconvoluted ³¹P MAS NMR spectrum of TMPO adsorbed on Sn-BEA (black), fitted cumulative peak (red) and single fitted peaks (green). Figure S11. Difference FTIR spectra of Sn-BEA (1), DeAl-BEA (2) and BEA (3) following pyridine adsorption. Figure S12. The OH-region of the difference FTIR spectra of Sn-BEA (1) and DeAl-BEA (2) zeolites following pyridine adsorption. Figure S13. FTIR spectra of the selected exhaust gases, 5000 ppm of CO₂ (1), 1000 ppm of NO₂ (2), 5000 ppm of CO (3), 5000 ppm of NO (4), water vapour (5). Figure S14. FTIR spectra of CO detected by Sn-BEA: 200 ppm (black), 400 ppm, 800 ppm, 1600 ppm, 3200 ppm, 4000 ppm, 4500 ppm, 5000 ppm. Figure S15. FTIR spectra of CO₂ detected by Sn-BEA: 200 ppm (black), 200-1000 ppm increments of 200 ppm, 1000-5000 ppm increments of 500 ppm. Figure S16. FTIR spectra of NO detected by Sn-BEA: 200 ppm (black), 400 ppm, 800 ppm, 1600 ppm, 3200 ppm, 5000 ppm. Figure S17. FTIR spectra of NO₂ detected by Sn-BEA: 50 ppm (black), 100-900 ppm increments of 100 ppm. Figure S18. FTIR spectra of CO detected by DeAl-BEA: 50 ppm (black), 100 ppm, 200 ppm, 300 ppm, 400 ppm, 600 ppm. Figure S19. FTIR spectra of CO₂ detected by DeAl-BEA: 1350 ppm (black), increments of 150 ppm. Figure S20. FTIR spectra of CO₂ detected by DeAl-BEA: zoomed in the 2450-2240 cm⁻¹ region, 1350 ppm (black), increments of 150 ppm, CO₂ gas phase spectrum subtracted. Figure S21. FTIR spectra NO detected by DeAl-BEA: 75 ppm (black), 100 ppm, 200 ppm, 400 ppm, 600 ppm. Figure S22. FTIR spectra of NO₂ detected by DeAl-BEA: 50 ppm (black), 75 ppm, 100 ppm, 200 ppm, 400 ppm, 600 ppm. Figure S23. FTIR spectra of 5000 ppm of H₂O (1), 5000 ppm of CO (2), 5000 ppm of NO (3), 5000 ppm of CO₂ (4) and 900 ppm of NO₂ (5) adsorbed on Sn-BEA, all the spectra are offset and spectrum 1 is multiplied by a factor of 0.1 for clarity. Figure S24. FTIR spectra of 5000 ppm of H₂O (1), 600 ppm of CO (2), 600 ppm of NO (3), 2050 ppm of CO₂ (4) and 600 ppm of NO₂ (5) adsorbed on DeAl-BEA, all the spectra are offset and spectrum 1 is multiplied by a factor of 0.1 for clarity. Figure S25. FTIR spectra of 900 ppm of NO₂ adsorbed on Sn-BEA (1), followed by desorption at room temperature for 30 min (2), 60 min (3) and 90 min (4).

Author Contributions: Conceptualisation, M.J., J.G., L.L., S.M. and V.Z.; Methodology, M.J., J.G., L.L., F.D., P.B. and V.Z.; Formal Analysis, M.J. and V.Z.; Investigation, M.J. and F.D.; Resources, S.M. and V.Z.; Data Curation, M.J.; Writing—Original Draft Preparation, M.J.; Writing—Review and Editing, L.L., S.M. and V.Z.; Visualization, M.J.; Supervision, J.G., L.L., P.B., J.E.F., S.M. and V.Z.; Project Administration, S.M. and V.Z.; Funding Acquisition, S.M. and V.Z. All authors have read and agreed to the published version of the manuscript.

Funding: M.J.'s Ph.D. has been funded by the Royal Society (IE160562), Keele University (KU-T6316), and the Newton Fund (Grant #261867079).

Institutional Review Board Statement: Not applicable.

Informed Consent Statement: Not applicable.

Data Availability Statement: <https://researchdata.keele.ac.uk/> (will be accessed on 20 February 2023).

Acknowledgments: S.M. and L.L. thank the Centre of Nanozeolites and Related Porous Materials, Région Normandie, CNRS (CLEAR) for supporting this work. M.J. would like to thank the Royal Society, Keele University, and the Newton Fund for funding his Ph.D. project, as well as Keele University and Normandie Université ENSICAEN staff for the help provided during the project.

Conflicts of Interest: The authors declare no conflict of interest.

References

1. WHO-OEHT. *WHO AIR Quality Guidelines for Particulate Matter, Ozone, Nitrogen Dioxide and Sulfur Dioxide*; WHO: Geneva, Switzerland, 2006.
2. European Environment Agency (EEA). *Air Quality in Europe—2020 Report*; EEA: Copenhagen, Denmark, 2020.
3. Sassykova, L.R.; Aubakirov, Y.A.; Sendilvelan, S.; Tashmukhambetova, Z.K.; Faizullaeva, M.F.; Bhaskar, K.; Batyrbayeva, A.A.; Ryskaliyeva, R.G.; Tyussyupova, B.B.; Zhakupova, A.A.; et al. The Main Components of Vehicle Exhaust Gases and Their Effective Catalytic Neutralization. *Orient. J. Chem.* **2019**, *35*, 110–127. [[CrossRef](#)]
4. Department for Environment Food and Rural Affairs. What Are the Causes of Air Pollution Pollutant Description and Main UK Sources Potential Effects on Health/Environment Particulate. 2011. Available online: https://uk-air.defra.gov.uk/assets/documents/What_are_the_causes_of_Air_Pollution.pdf (accessed on 17 January 2023).
5. Wadhvani, P.; Yadav, S. *Gas Sensors Market Size & Share—Global Forecasts 2026*; GMI Pulse: Selbyville, DE, USA, 2020.
6. Fergus, J.W. Materials for high temperature electrochemical NO_x gas sensors. *Sens. Actuators B Chem.* **2007**, *121*, 652–663. [[CrossRef](#)]
7. Park, C.O.; Fergus, J.W.; Miura, N.; Park, J.; Choi, A. Solid-state electrochemical gas sensors. *Ionics* **2009**, *15*, 261–284. [[CrossRef](#)]
8. Gardon, M.; Guilemany, J.M. A review on fabrication, sensing mechanisms and performance of metal oxide gas sensors. *J. Mater. Sci. Mater. Electron.* **2013**, *24*, 1410–1421. [[CrossRef](#)]
9. Wang, C.; Yin, L.; Zhang, L.; Xiang, D.; Gao, R. Metal oxide gas sensors: Sensitivity and influencing factors. *Sensors* **2010**, *10*, 2088–2106. [[CrossRef](#)]
10. Dey, A. Semiconductor metal oxide gas sensors: A review. *Mater. Sci. Eng. B Solid-State Mater. Adv. Technol.* **2018**, *229*, 206–217. [[CrossRef](#)]
11. Dinh, T.-V.; Choi, I.-Y.; Son, Y.-S.; Kim, J.-C. A review on non-dispersive infrared gas sensors: Improvement of sensor detection limit and interference correction. *Sens. Actuators B* **2016**, *231*, 529–538. [[CrossRef](#)]
12. Cejka, J.; van Bekkum, H.; Corma, A.; Schuth, F. (Eds.) *Introduction to Zeolite Science and Practice*; Elsevier Science: Amsterdam, The Netherlands, 2007.
13. Talapaneni, S.N.; Grand, J.; Thomas, S.; Ahmad, H.A.; Mintova, S. Nanosized Sn-MFI zeolite for selective detection of exhaust gases. *Mater. Des.* **2016**, *99*, 574–580. [[CrossRef](#)]
14. Xu, X.; Wang, J.; Long, Y. Zeolite-based Materials for Gas Sensors. *Sensors* **2006**, *6*, 1751–1764. [[CrossRef](#)]
15. Sahner, K.; Hagen, G.; Schönauer, D.; Reiß, S.; Moos, R. Zeolites—Versatile materials for gas sensors. *Solid State Ionics* **2008**, *179*, 2416–2423. [[CrossRef](#)]
16. Yang, P.; Ye, X.; Lau, C.; Li, Z.; Liu, X.; Lu, J. Design of Efficient Zeolite Sensor Materials for n-Hexane. *Anal. Chem.* **2007**, *79*, 1425–1432. [[CrossRef](#)]
17. Corma, A.; Cambor, M.A.; Esteve, P.; Martínez, A.; Pérez-Pariente, J. Activity of Ti-Beta Catalyst for the Selective Oxidation of Alkenes and Alkanes. *J. Catal.* **1994**, *145*, 151–158. [[CrossRef](#)]
18. Zhou, W.; Sun, P.; Navrotsky, A.; Kim, S.H.; Hong, S.B. Formation and dehydration enthalpies of gallosilicate materials with different framework topologies and Ga contents. *Microporous Mesoporous Mater.* **2009**, *121*, 200–207. [[CrossRef](#)]
19. Bui, L.; Luo, H.; Gunther, W.R.; Román-Leshkov, Y. Domino Reaction Catalyzed by Zeolites with Brønsted and Lewis Acid Sites for the Production of γ -Valerolactone from Furfural. *Angew. Chem. Int. Ed.* **2013**, *52*, 8022–8025. [[CrossRef](#)]
20. Luo, H.Y.; Consoli, D.F.; Gunther, W.R.; Román-Leshkov, Y. Investigation of the reaction kinetics of isolated Lewis acid sites in Beta zeolites for the Meerwein–Ponndorf–Verley reduction of methyl levulinate to γ -valerolactone. *J. Catal.* **2014**, *320*, 198–207. [[CrossRef](#)]
21. Lewis, J.D.; Van de Vyver, S.; Román-Leshkov, Y. Acid–Base Pairs in Lewis Acidic Zeolites Promote Direct Aldol Reactions by Soft Enolization. *Angew. Chem. Int. Ed.* **2015**, *54*, 9835–9838. [[CrossRef](#)] [[PubMed](#)]
22. Corma, A.; Nemeth, L.T.; Renz, M.; Valencia, S. Sn-zeolite beta as a heterogeneous chemoselective catalyst for Baeyer–Villiger oxidations. *Nature* **2001**, *412*, 423–425. [[CrossRef](#)] [[PubMed](#)]
23. Hwang, S.J.; Gounder, R.; Bhawe, Y.; Orazov, M.; Bermejo-Deval, R.; Davis, M.E. Solid State NMR Characterization of Sn-Beta Zeolites that Catalyze Glucose Isomerization and Epimerization. *Top. Catal.* **2015**, *58*, 435–440. [[CrossRef](#)]

24. Bermejo-De Val, R.; Assary, R.S.; Nikolla, E.; Moliner, M.; Roman-Leshkov, Y.; Hwang, S.-J.; Palsdottir, A.; Silverman, D.; Lobo, R.F.; Curtiss, L.A.; et al. Metalloenzyme-like catalyzed isomerizations of sugars by Lewis acid zeolites. *Proc. Natl. Acad. Sci. USA* **2012**, *109*, 9727–9732. [[CrossRef](#)]
25. Moliner, M.; Román-Leshkov, Y.; Davis, M.E. Tin-containing zeolites are highly active catalysts for the isomerization of glucose in water. *Proc. Natl. Acad. Sci. USA* **2010**, *107*, 6164–6168. [[CrossRef](#)]
26. Roman-Leshkov, Y.; Moliner, M.; Labinger, J.A.; Davis, M.E. Mechanism of glucose isomerization using a solid lewis acid catalyst in water. *Angew. Chem. Int. Ed.* **2010**, *49*, 8954–8957. [[CrossRef](#)] [[PubMed](#)]
27. Taarning, E.; Saravanamurugan, S.; Holm, M.S.; Xiong, J.; West, R.M.; Christensen, C.H. Zeolite-Catalyzed Isomerization of Triose Sugars. *ChemSusChem* **2009**, *2*, 625–627. [[CrossRef](#)]
28. Dijkmans, J.; Gabriëls, D.; Dusselier, M.; de Clippel, F.; Vanelderen, P.; Houthoofd, K.; Malfliet, A.; Pontikes, Y.; Sels, B.F. Productive sugar isomerization with highly active Sn in dealuminated β zeolites. *Green Chem.* **2013**, *15*, 2777–2785. [[CrossRef](#)]
29. Zhu, Z.; Xu, H.; Jiang, J.; Liu, X.; Ding, J.; Wu, P. Postsynthesis of FAU-type stannosilicate as efficient heterogeneous catalyst for Baeyer-Villiger oxidation. *Appl. Catal. A Gen.* **2016**, *519*, 155–164. [[CrossRef](#)]
30. Harris, J.W.; Liao, W.-C.; Di Iorio, J.R.; Henry, A.M.; Ong, T.-C.; Comas-Vives, A.; Copéret, C.C.; Gounder, R.; Davidson, C.D. Molecular Structure and Confining Environment of Sn Sites in Single-Site Chabazite Zeolites. *Chem. Mater.* **2017**, *29*, 8824–8837. [[CrossRef](#)]
31. Skeels, G.W.; Flanigen, E.M. Zeolite Chemistry VII-Framework Substitution for Aluminum in Zeolites VIA Secondary Synthesis Treatment. *Stud. Surf. Sci. Catal.* **1989**, *49*, 331–344.
32. Gunther, W.R.; Wang, Y.; Ji, Y.; Michaelis, V.K.; Hunt, S.T.; Griffin, R.G.; Román-Leshkov, Y. Sn-Beta zeolites with borate salts catalyze the epimerization of carbohydrates via an intramolecular carbon shift. *Nat. Commun.* **2012**, *3*, 1109. [[CrossRef](#)] [[PubMed](#)]
33. Yakimov, A.V.; Kolyagin, Y.G.; Tolborg, S.; Vennestrøm, P.N.R.; Ivanova, I.I. Accelerated synthesis of Sn-BEA in fluoride media: Effect of H₂O content in the gel. *New J. Chem.* **2016**, *40*, 4367–4374. [[CrossRef](#)]
34. Chang, C.-C.; Wang, Z.; Dornath, P.; Cho, H.J.; Fan, W. Rapid synthesis of Sn-Beta for the isomerization of cellulosic sugars. *RSC Adv.* **2012**, *2*, 10475–10477. [[CrossRef](#)]
35. Harris, J.W.; Cordon, M.J.; Di Iorio, J.R.; Vega-Vila, J.C.; Ribeiro, F.H.; Gounder, R. Titration and quantification of open and closed Lewis acid sites in Sn-Beta zeolites that catalyze glucose isomerization. *J. Catal.* **2016**, *335*, 141–154. [[CrossRef](#)]
36. Boronat, M.; Concepción, P.; Corma, A.; Renz, M.; Valencia, S. Determination of the catalytically active oxidation Lewis acid sites in Sn-beta zeolites, and their optimisation by the combination of theoretical and experimental studies. *J. Catal.* **2005**, *234*, 111–118. [[CrossRef](#)]
37. Sushkevich, V.L.; Ivanova, I.I.; Yakimov, A.V. Revisiting Acidity of SnBEA Catalysts by Combined Application of FTIR Spectroscopy of Different Probe Molecules. *J. Phys. Chem. C* **2017**, *121*, 11437–11447. [[CrossRef](#)]
38. Lewis, J.D.; Ha, M.; Luo, H.; Faucher, A.; Michaelis, V.K.; Román-Leshkov, Y. Distinguishing Active Site Identity in Sn-Beta Zeolites Using ³¹P MAS NMR of Adsorbed Trimethylphosphine Oxide. *ACS Catal.* **2018**, *8*, 3076–3086. [[CrossRef](#)]
39. Josephson, T.R.; Jenness, G.R.; Vlachos, D.G.; Caratzoulas, S. Distribution of open sites in Sn-Beta zeolite. *Microporous Mesoporous Mater.* **2017**, *245*, 45–50. [[CrossRef](#)]
40. Freitas, C.; Barrow, N.; Zholobenko, V. Accessibility and Location of Acid Sites in Zeolites as Probed by Fourier Transform Infrared Spectroscopy and Magic Angle Spinning Nuclear Magnetic Resonance. *Johns. Matthey Technol. Rev.* **2018**, *62*, 279–290. [[CrossRef](#)]
41. Zholobenko, V.; Freitas, C.; Jendrlin, M.; Bazin, P.; Travert, A.; Thibault-Starzyk, F. Probing the acid sites of zeolites with pyridine: Quantitative AGIR measurements of the molar absorption coefficients. *J. Catal.* **2020**, *385*, 52–60. [[CrossRef](#)]
42. Kobler, J.; Abrevaya, H.; Mintova, S.; Bein, T. High-Silica Zeolite- β : From Stable Colloidal Suspensions to Thin Films. *J. Phys. Chem. C* **2008**, *112*, 14274–14280. [[CrossRef](#)]
43. Sushkevich, V.L.; Kots, P.A.; Kolyagin, Y.G.; Yakimov, A.V.; Marikutsa, A.V.; Ivanova, I.I. Origin of Water-Induced Brønsted Acid Sites in Sn-BEA Zeolites. *J. Phys. Chem. C* **2019**, *123*, 5540–5548. [[CrossRef](#)]
44. Van de Vyver, S.; Odermatt, C.; Romero, K.; Prasomsri, T.; Román-Leshkov, Y. Solid Lewis Acids Catalyze the Carbon–Carbon Coupling between Carbohydrates and Formaldehyde. *ACS Catal.* **2015**, *5*, 972–977. [[CrossRef](#)]
45. Pacheco, J.J.; Davis, M.E. Synthesis of terephthalic acid via Diels-Alder reactions with ethylene and oxidized variants of 5-hydroxymethylfurfural. *Proc. Natl. Acad. Sci. USA* **2014**, *111*, 8363–8367. [[CrossRef](#)]
46. Holm, M.S.; Pagán-Torres, Y.J.; Saravanamurugan, S.; Riisager, A.; Dumesic, J.A.; Taarning, E. Sn-Beta catalysed conversion of hemicellulosic sugars. *Green Chem.* **2012**, *14*, 702–706. [[CrossRef](#)]
47. Bermejo-Deval, R.; Gounder, R.; Davis, M.E. Framework and Extraframework Tin Sites in Zeolite Beta React Glucose Differently. *ACS Catal.* **2012**, *2*, 2705–2713. [[CrossRef](#)]
48. Hammond, C.; Conrad, S.; Hermans, I. Simple and Scalable Preparation of Highly Active Lewis Acidic Sn- β . *Angew. Chem. Int. Ed.* **2012**, *51*, 11736–11739. [[CrossRef](#)] [[PubMed](#)]
49. Treacy, M.M.J.; Higgins, J.B. (Eds.) *Collection of Simulated XRD Powder Patterns for Zeolites*; Elsevier: Amsterdam, The Netherlands, 2001.
50. Al-Ani, A.; Haslam, J.J.C.; Mordvinova, N.E.; Lebedev, O.I.; Vicente, A.; Fernandez, C.; Zholobenko, V. Synthesis of nanostructured catalysts by surfactant-lating of large-pore zeolites. *Nanoscale Adv.* **2019**, *1*, 2029–2039. [[CrossRef](#)]

51. Protsak, I.S.; Morozov, Y.M.; Dong, W.; Le, Z.; Zhang, D.; Henderson, I.M. A ^{29}Si , ^1H , and ^{13}C Solid-State NMR Study on the Surface Species of Various Depolymerized Organosiloxanes at Silica Surface. *Nanoscale Res. Lett.* **2019**, *14*, 160. [[CrossRef](#)] [[PubMed](#)]
52. Dubray, F.; Moldovan, S.; Kouvatias, C.; Grand, J.; Aquino, C.; Barrier, N.; Gilson, J.-P.; Nesterenko, N.; Minoux, D.; Mintova, S. Direct Evidence for Single Molybdenum Atoms Incorporated in the Framework of MFI Zeolite Nanocrystals. *J. Am. Chem. Soc.* **2019**, *141*, 8689–8693. [[CrossRef](#)]
53. Zheng, A.; Liu, S.-B.; Deng, F. ^{31}P NMR Chemical Shifts of Phosphorus Probes as Reliable and Practical Acidity Scales for Solid and Liquid Catalysts. *Chem. Rev.* **2017**, *117*, 12475–12531. [[CrossRef](#)]
54. Ohlin, L.; Berezovsky, V.; Öberg, S.; Farzaneh, A.; Holmgren, A.; Grahn, M. Effect of Water on the Adsorption of Methane and Carbon Dioxide in Zeolite Na-ZSM-5 Studied Using in Situ ATR-FTIR Spectroscopy. *J. Phys. Chem. C* **2016**, *120*, 29144–29152. [[CrossRef](#)]
55. Wang, Z.-M.; Arai, T.; Kumagai, M. Cooperative and Competitive Adsorption Mechanism of NO_2 , NO , and H_2O on H-Type Mordenite. *Ind. Eng. Chem. Res.* **2001**, *40*, 1864–1871. [[CrossRef](#)]
56. Ohlin, L.; Bazin, P.; Frédé, F.; Thibault-Starzyk, F.; Hedlund, J.; Grahn, M. Adsorption of CO_2 , CH_4 , and H_2O in Zeolite ZSM-5 Studied Using in Situ ATR-FTIR Spectroscopy. *J. Phys. Chem. C* **2013**, *117*, 16972–16982. [[CrossRef](#)]
57. Szanyi, J.; Kwak, J.H.; Moline, R.A.; Peden, C.H.F. The adsorption of NO_2 and the $\text{NO}+\text{O}_2$ reaction on Na-Y, FAU: An in situ FTIR investigation. *Phys. Chem. Chem. Phys.* **2003**, *5*, 4045–4051. [[CrossRef](#)]
58. Szanyi, J.; Kwak, J.H.; Peden, C.H.F. The Effect of Water on the Adsorption of NO_2 in Na- and Ba-Y, FAU Zeolites: A combined FTIR and TPD Investigation. *J. Phys. Chem. B* **2004**, *108*, 3746–3753. [[CrossRef](#)]
59. Hadjiivanov, K.I. Identification of neutral and charged N_xO_y surface species by IR spectroscopy. *Catal. Rev. Sci. Eng.* **2000**, *42*, 71–144. [[CrossRef](#)]
60. Santhosh Kumar, M.; Schwidder, M.; Grunert, W.; Bentrup, U.; Brückner, A. Selective reduction of NO with Fe-ZSM-5 catalysts of low Fe content: Part II. Assessing the function of different Fe sites by spectroscopic in situ studies. *J. Catal.* **2006**, *239*, 173–186. [[CrossRef](#)]
61. Brosius, R.; Bazin, P.; Thibault-Starzyk, F.; Martens, J.A. Operando FTIR study of reaction pathways of selective catalytic reduction of NO_x with decane in the presence of water on iron-exchanged MFI-type zeolite. *J. Catal.* **2005**, *234*, 191–198. [[CrossRef](#)]
62. Ahrens, M.; Marie, O.; Bazin, P.; Daturi, M. Fe-H-BEA and Fe-H-ZSM-5 for NO_2 removal from ambient air—A detailed in situ and operando FTIR study revealing an unexpected positive water-effect. *J. Catal.* **2010**, *271*, 1–11. [[CrossRef](#)]

Disclaimer/Publisher’s Note: The statements, opinions and data contained in all publications are solely those of the individual author(s) and contributor(s) and not of MDPI and/or the editor(s). MDPI and/or the editor(s) disclaim responsibility for any injury to people or property resulting from any ideas, methods, instructions or products referred to in the content.